Journal of Materials Processing Tech. 343 (2025) 118959

Contents lists available at ScienceDirect

Journal of Materials Processing Tech.

journal homepage: www.elsevier.com/locate/jmatprotec

Research Article

Elucidating the role of ordered phases and carbides in the mechanical performance of friction stir welded high aluminum low-density ferrite steels

Junqi Chen, Takuya Miura, Kohsaku Ushioda, Abhishek Sharma, Hidetoshi Fujii *

Joining and Welding Research Institute (JWRI), Osaka University, 11-1 Mihogaoka, Ibaraki, Osaka 567-0047, Japan

ARTICLE INFO

Keywords:
Friction stir welding
Fe-C-Al
DO_3 decomposition
Shearable κ-carbide

ABSTRACT

The widespread adoption of high-Al steels is hindered by weldability challenges due to thermal cracking susceptibility and coarse-grained phase transformations by traditional fusion welding. For the first time, we demonstrate an innovative low-temperature (<700°C) friction stir welding (FSW) for processing Fe-10Al and Fe-0.1C-10 (wt%) Al alloys. The X-ray diffraction (XRD) and transmission electron microscope (TEM) observations confirmed that the ultralow-rotation/high-load FSW process induces order phase DO_3 disordering by severe plastic deformation and κ-carbide shearing by gliding dislocations, collectively relieving stress concentrations while achieving ~6 μm grain refinement. This unique microstructural evolution promotes dislocation slip-dominated deformation and consequently superior strength-ductility synergy in high-Al steels compared to the existing methods. Quantitatively, the small sized specimens of Fe-10Al alloy exhibited a tensile strength of ~684 MPa with a total elongation of ~40 %, local elongation around 28 %, and an impact upper shelf energy of ~390 kJ/m^2 with a DBTT of –15 °C. Meanwhile, the Fe-0.1C-10Al alloy achieved a higher strength of ~725 MPa and a total elongation of ~38 %, along with an upper shelf energy of 454 kJ/m^2. However, due to the presence of residual κ-carbides and DO_3, faster crack propagation occurred during impact testing, resulting in an increased DBTT (~70 °C). The study establishes new FSW parameter-design principles for manufacturing high-performance high-Al steel components.

1. Introduction

The demand for lightweight steel in structural applications continues to grow, particularly in the automotive and transportation sectors. This trend arises from the pressing need to improve fuel efficiency, lower carbon emissions, enhance strength-to-weight ratios, and ensure high safety standards [1,2]. The addition of lightweight elements such as Li, Mg, Al, Si, etc. through alloying significantly reduces the density of steel. Among these, Al [3] has emerged as the key element in the development of low-density Fe-Al alloys due to its exceptional performance in reducing density, enhancing strength, and providing corrosion resistance as well as high temperature oxidation resistance [4]. However, the onset of ordering reactions occurs at approximately 5 wt% Al content. The structure transitions from a disordered state to the intermediate K-state (~6 wt% Al) and subsequently to the ordered structures DO_3 (~10 wt% Al) and B2 (~22 wt% Al) as the Al content increases [5]. These transformations influence the strength, ductility, toughness, and elastic properties of the materials, caused by the ordered DO_3 and B2 superlattice structures, which exhibit brittle characteristics [6].

For Fe-Al alloys with an Al content exceeds 20 at%, DO_3 or B2 ordered structure forms depending on the Al content and temperature, the relationship between mechanical properties has been extensively reported and studied in detail [7,8]. Where, the A_3B (Fe_3Al)) type as the perfect order of DO_3-phase with cubic structure (Lattice parameter: 0.5792 nm; Space group: Fm-3m) is regarded as an ordered arrangement based on the disordered A2 (body-centered cube, BCC) structure. Nucleation and growth of the classical DO_3 phase from a ferrite ($\alpha \rightarrow DO_3$) was observed in the report of Morris et al. [9]. The ordered DO_3 phase restricts dislocation slip through pinning effects, and its dominance with increasing Al content significantly enhances the tensile and yield strengths of Fe-Al ferrite-based alloys but is accompanied by a sharp decline in total elongation and a transition in fracture mode from ductile to brittle fracture without necking [10]. The local elongation drops to nearly 0 % as the Al content reaches 10 wt% [4]. Consequently,

* Corresponding author.
E-mail address: fujii.hidetoshi.jwri@osaka-u.ac.jp (H. Fujii).

https://doi.org/10.1016/j.jmatprotec.2025.118959
Received 9 May 2025; Received in revised form 26 June 2025; Accepted 1 July 2025
Available online 2 July 2025

the current Al content in ferrite-based Fe-Al alloys is presumed to be strongly limited.

Whereas in Fe-C-Al ternary alloys, the type of carbides precipitated varies with the Al content [11]. These precipitates serve as an obstacle to the dislocation motion and form the foundation of precipitation hardening mechanism for enhancing the strength of metallic materials [12]. This process generally occurs in two modes [13]: dislocations either cutting through semi-coherent or coherent-lattice particles at higher stresses or bypassing impenetrable precipitates via Orowan loops, also requiring stress increment. The Orowan looping mechanism, although providing notable strengthening, involves dislocation accumulation around impenetrable particles, leading to stress concentration and consequently leading to the risk of particle cracking [14]. Furthermore, this stress concentration often renders the interface between the matrix and hard particles vulnerable to crack initiation, significantly compromising the ductility and damage tolerance of material under stress. This trade-off has driven efforts to introduce coherent nano-precipitates into alloys as a facilitation to balance strength and ductility synergy [15,16]. Nevertheless, this method typically entails a highly intricate and controlled processing route. Challenging this conventional approach, the shearable κ-carbide precipitates was intentionally introduced with an objective of getting dual benefits [11]: the strengthening and strain-hardening effects associated with dislocation bowing, and the enhanced ductility effect resulting from stress relaxation during dislocation cutting through these precipitates.

Notably, friction stir welding (FSW) [17], as a unique and intense thermo-mechanical process, has the potential to decompose the DO_3 phase and generate a high density of dislocations capable of shearing κ-carbides, thereby readily enhancing the mechanical properties of Fe-Al and Fe-C-Al alloys with high Al content. In contrast, conventional fusion welding techniques [18] generally involve high heat input — for instance, gas tungsten arc (GTA) welding typically operates in the range of 270–1466 $J{\cdot}mm^{-1}$ [19]. Such excessive thermal input often leads to severe microstructural coarsening and a high risk of solidification cracking in the fusion zone, both of which contribute to brittleness and degraded joint performance. Based on this, Ku et al. [20] and Tjong et al. [21] attempted to employ relatively lower heat input fusion welding methods, such as electron beam and continuous wave CO_2 laser welding, to join Fe-28Mn-(5,6)Al-1C alloys. However, the resulting welds still showed significantly inferior strength and toughness compared to the base metal. Microstructural characterization revealed minor Al microsegregation in interdendritic regions, as well as a mixture of columnar and equiaxed austenite, which collectively accounted for the poor mechanical performance. To the best of our knowledge, there are no previous studies successfully applying fusion welding techniques to high-Al steels with satisfactory mechanical outcomes.

By comparison, FSW, as a solid-state welding process, effectively avoids the issues associated with fusion-based methods — particularly solidification cracking and weld zone coarsening. Its ability to maintain a relatively low peak temperature while inducing intense plastic deformation makes it an especially suitable technique for joining high-Al steels. By employing optimized parameters (rotational rate: 80 rpm; traveling speed: 100 mm/min; axial force: 40 kN), this process achieves effective joining at low peak welding temperatures below 700 ℃, significantly refining dynamically recrystallized grain, strongly affecting DO_3 and κ-carbide, which are expected to result in the novel properties of ferrite-based high-Al alloys [17]. In other words, this leads to a desirable combination of strength and toughness in the stir zone (SZ), accompanied by an improvement in local elongation [22]. On the other hand, comparative analysis indicates that SZ specimens of the Fe-0.1C-5Al alloy exhibit enhanced strength, ductility, and toughness compared to those of the Fe-0.1C-0.05Al alloy. These improvements are attributed to the distinct deformation behaviors of cementite and κ-carbide under the thermo-mechanical conditions inherent to the FSW process [11]. Consequently, the metallurgical concept realized by the unique FSW process using 10 wt%Al alloys is expected to be applied to manufacture high-Al base metal products having novel properties. However, to date, no studies have explored the FSW of high-Al (~10 wt %) ferritic steels and their mechanical performance under conditions not exceeding peak temperature 700℃.

To fill this gap, this study systematically investigates the microstructural evolution and mechanical behavior of the stir zones (SZs) in FSWed Fe-10Al and Fe-0.1C-10Al (wt%) alloys, with a particular focus on the responses of the ordered DO_3 phase and κ-carbides. This work, for the first time, demonstrates that excellent strength, ductility, and toughness synergy in SZ of high-Al steels can be achieved by carefully tailoring the FSW parameters. Furthermore, this approach shows promise for broader application to other high-Al or high-alloy steels. Overall, this study addresses a key research gap and proposes a novel strategy for solid-state joining of brittle high-Al ferritic steel.

2. Experimental procedure

2.1. Materials preparation and friction stir welding

The thermomechanical processing route in this study is illustrated in schematic Fig. 1f. Fe-10Al and Fe-0.1C-10Al alloy ingots with 350 gf were melted using a high-frequency vacuum induction furnace. Prior to hot rolling, the ingots were inserted into the box furnace and preheated at 700 ℃ for 10 min. Multi-pass hot rolling was then performed on the ingots to reduce the final thickness to 3.4 mm. The ingots were heated at 700℃ for 10 min before each pass to maintain a consistent hot rolling temperature. The rolled plates were subsequently annealed at 700 °C for 30 min followed by air cooling. Following annealing, the plates were milled on both the surfaces to remove the oxide scale and obtain a final plate of 3 mm thickness for subsequent FSW. The final dimensions of the plates for FSW include a length of approximately 200 mm, a width of approximately 40 mm, and a thickness of 3 mm.

The schematic of the FSW process is shown in Fig. 1b. To ensure a ferrite-based microstructure, the peak welding temperature was intentionally controlled at a low temperature within the ferrite phase region (~700 °C) [23]. The welding parameters were set as follows: significantly low tool rotational rate of 80 rpm, traveling speed of 100 mm/min, and axial force of 40 kN, respectively. Importantly, a constant relatively high axial force was maintained during the entire welding process at a low temperature, as verified by the pressure recording and thermal cycle shown in the insets of Fig. 1b. The axis load was constantly maintained at 40 kN, and the peak temperature remained below 700 °C to achieve (1) minimized heat input, and (2) enhanced shear deformation. The welding tool was fabricated from cemented tungsten carbide (WC) (FSW7, Sanalloy, Japan), with a shoulder diameter of 15 mm, a pin diameter of 6 mm, and a pin length of 2.9 mm, as shown in Fig. 1c. The tool tilt angle along the transverse direction was maintained at 3°. The entire FSW process was conducted under an argon atmosphere (20 L/min.) to prevent oxidation of the weld surface. Fig. 1d shows the macroscopic appearance of the steel plate surface and cross-sectional morphology of joints after FSW under load control, displaying without macroscopic inclusions, undercuts, and pores. The subsequent microstructure observations and mechanical testing prove that sound joints were obtained for high Al alloys of 10 wt%.

2.2. Microstructural analysis

Specimens for microstructural characterization and mechanical testing were sectioned using electrical discharge machining (EDM). Microstructural observations were conducted using a field-emission scanning electron microscope (FE-SEM; JEOL JSM-7001FA) and a transmission electron microscope (TEM; JEOL 2011 F). SEM specimens were mechanically polished and etched with a solution of 4.0 % nitric acid in 96.0 % ethanol, followed by ultrasonic cleaning before examination. Analyses of grain size, deformation mechanism, and crack propagation were performed using an electron backscatter diffraction

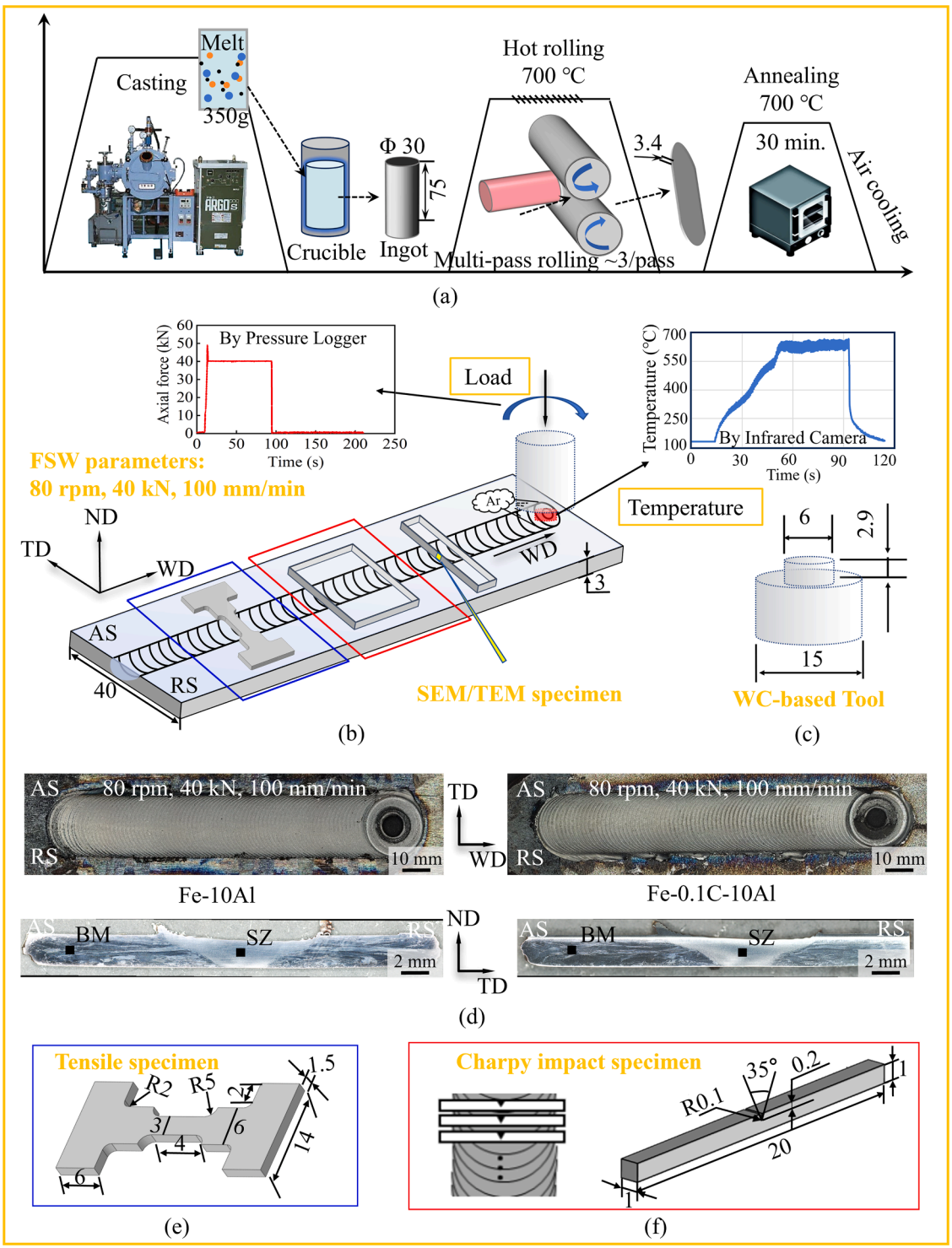

Fig. 1. Schematic illustration of the matrix plates preparation procedure, the FSW process, sampling positions, geometry and dimension of specimen (Unit: mm), and the weld/joint cross-sectional morphologies. (a) Casting, hot rolling, and annealing conditions for Fe-10Al and Fe-0.1C-10Al alloys. (b) Diagram of the FSW process at 80 rpm, 40 kN, and 100 mm/min. The inset shows the pressure (constant at 40 kN) and thermal cycle during welding, with peak temperature below 700 °C. Sampling locations for tensile (blue box) and mini Charpy impact specimens (red box) are indicated. (c) Geometry and dimension of the WC tool used in FSW. (d) Surface appearance and cross-sectional morphology of joints produced on Fe-10Al and Fe-0.1C-10Al plates under the above FSW conditions, showing defect-free joints. (e) Dimension of the non-standard tensile specimen. (f) Dimension of the miniaturized Charpy impact specimen.

(EBSD) system integrated with the SEM. EBSD specimens were mechanically polished and subsequently treated with an oxide polishing suspension (OPS) to remove residual surface deformation and mechanical stress. The acquired EBSD data were processed using TSL OIM analysis software.

TEM specimens were prepared using a focused ion beam (FIB) milling process with an FEI Helios NanoLab 600 dual-beam system. The FIB-selected regions were located at the center of the SZ, as indicated by the yellow box of the SEM/TEM specimen in Fig. 1b. For carbon-containing alloys, FIB milling was performed at the midsection of the

carbide particles, ensuring that the upper region of the TEM specimen contained carbides with a sufficiently thin thickness (~50–70 nm) for detailed microstructural analysis.

Phase identification was conducted using X-ray diffraction (XRD, RIGAKU-ULTIMA IV) in addition to TEM analysis. The XRD measurements included both broad-range scans (Step size: 0.05°) and high-resolution scans for selected regions (Step size: 0.01°).

2.3. Mechanical property tests

Microhardness distribution was evaluated using the same SEM specimens with a Vickers hardness tester (FM-800, FUTURE-TECH) under a load of ~2.94 N (HV0.3) and a dwell time of 15 s. Indentation spacing was maintained at 0.3 mm.

Tensile specimens were obtained perpendicular to the welding direction. Tensile specimens were prepared as non-standard dog-bone-shaped small specimens, with dimensions provided in Fig. 1e. All specimens were mechanically polished to eliminate surface defects or irregularities. The tensile strength evaluation was performed by a universal tensile test machine (AGS-X, SHIMADZU, Japan) with a 10 kN load capacity at a constant crosshead displacement rate of 0.2 mm/min at room temperature. A digital image correlation (DIC) system was employed for strain monitoring by the application of a speckle pattern. Images were captured at a frequency of 500 ms and synchronized with the load-displacement data. Each tensile test was conducted at room temperature, with three repeated tests per condition to ensure reproducibility. The displacement field and strain were analyzed using Vic-3D software [24].

Charpy impact tests were conducted (Tanaka, MI20T-D05KJ type) with a temperature range from −120 °C to 120 °C and the impact velocity was 60 m/min. The specimens were non-standard V-notched specimens with dimensions of 1 × 1 × 20 mm and a notch depth of 0.2 mm, as shown in Fig. 1f.

3. Results

3.1. Microstructures of base metal and stir zone

The secondary electronic image (SEI) morphologies of the base metals (BM) (Figs. 2a,d1) and the SZs (Figs. 2b,e1) of Fe-10Al and Fe-0.1C-10Al alloys, as well as the inverse pole figure (IPF) maps of the SZs (Fig. 2c,f), are presented. Coarse ferrite grains appear highly elongated due to multi-pass hot rolling in the BMs of Fe-10Al and Fe-0.1C-10Al. Dynamic recrystallization (DRX) induced by FSW refines the ferrite grains (Fig. 2b) with an average equiaxed ferrite grain size of approximately 5.0 μm in the SZ of Fe-10Al (Fig. 2c). The addition of 0.1 wt% C to the Fe-10Al alloy results in the precipitation of coarse carbides within the ferrite matrix of BM, as shown in Fig. 2d1. The enlarged view of the red-marked region in Fig. 2d1 is displayed in Fig. 2d2. SEM-EDS line scans confirm that the precipitated carbides are κ-carbides, with a noticeable Al-depleted region surrounding the larger κ-carbide particles. The calculated phase diagram suggests that κ-carbides can exist over a broad composition and temperature range [1,17]. It is well known that excess Al promotes the thermodynamic stabilization of κ-carbides. With the addition of 10 wt% Al, the precipitated κ-carbides have an average size of approximately 2.5 μm, which is larger than those at 5 wt% Al (0.6 μm) [17]. As the Al content increases, a higher fraction of relatively large κ-carbide particles tends to precipitate. This phenomenon was also reported in previous studies on the microstructure and mechanical properties of FeMnAlC alloy weld heat-affected zones [25]. After FSW, the ferrite grain size is refined to 6.1 μm (Fig. 2f), and large κ-carbides in SZ partially retained from the BM are evident (Fig. 2e1). Additionally, fine carbides are observed at grain boundaries, which EDS analysis identifies as κ-carbides (Fig. 2e1,

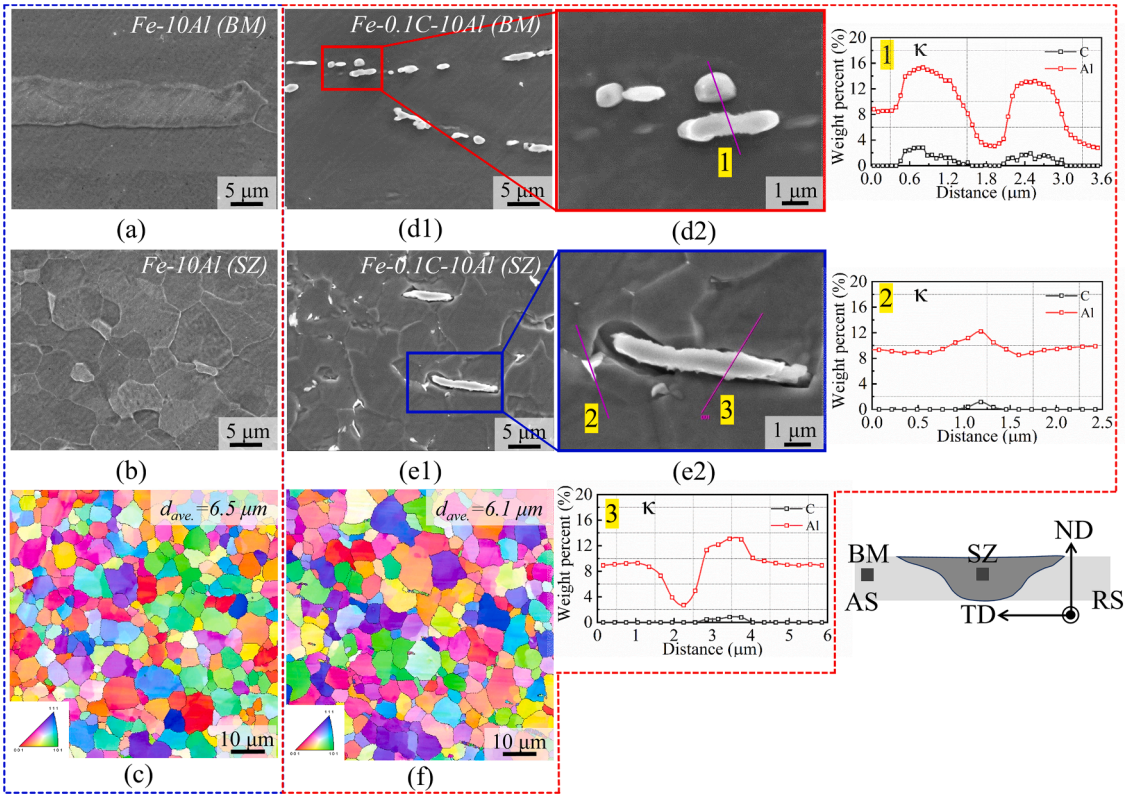

Fig. 2. Microstructure analysis of BM and SZ regions of Fe-10Al and Fe-0.1C-10Al alloys. (a, b) SEM images of the BM and SZ of Fe-10Al alloy, respectively. (c) The corresponding IPF maps of SZ in Fe-10Al alloy. (d1, e1) SEM images of the BM and SZ of Fe-0.1C-10Al alloy, respectively. (f) The corresponding IPF maps of SZ in Fe-0.1C-10Al alloy. (d2, e2) Magnified views of selected areas in (d1) and (e1) for EDS analysis of precipitated carbides, as shown in Area 1, 2, and 3.

with an enlarged view of the blue-boxed region in Fig. 2e2). Notably, the Al and C content in the measured κ-carbides is slightly lower than in the BM. During FSW, although κ-carbides exhibit some deformability, ferrite undergoes more substantial plastic deformation [11]. This strain incompatibility leads to the partial decohesion of κ-carbides and matrix.

On the other hand, given the high Al content (~10 wt%), the formation of the ordered DO_3 phase is expected. This was confirmed by XRD analysis as shown in Fig. 3. By comparing the Powder Diffraction File (PDF) cards of the ferrite matrix (PDF: 01–075–6499) and ordered Fe_3Al (PDF:00–033–0020), as provided by the International Centre for Diffraction Data (ICDD), it was found that most major ferrite peaks of the two alloys overlap significantly within the 2θ range of 20°~90°. The three strongest ferrite peaks appear at approximately 44.2° (110), 64.3° (200), 81.3° (211). A distinct characteristic peak of DO_3 appears at approximately $2\theta \approx 26°\sim27°$. To verify its presence, a high-resolution scan (Step size of 0.01°) was performed within this range, revealing a weak peak at ~26.8° in both the BM and SZ of Fe-10Al, speculating the existence of the DO_3 phase. Another verification of DO_3 by TEM observation is presented later in this paper. For the Fe-0.1C-10Al alloy, a detailed scan was conducted within the 2θ range of 41.0°~42.8° using a step size of 0.01°, presumably detecting a weak but characteristic peak corresponding to κ-carbide. Although faint, this peak is sufficient to confirm the presence of κ-carbides, aligning well with the microstructural observations and interpretations described earlier.

3.2. Hardness distribution

The hardness distributions of the BM and SZ in Fe-10Al and Fe-0.1C-10Al alloys are shown in Fig. 4. The BM hardnesses were 233 HV and 244 HV, respectively. The SZ hardnesses increased slightly to 242 HV and 256 HV despite significant grain refinement by FSW in Fe-10Al and Fe-0.1C-10Al alloys, respectively. Compared to the reported hardness variations in Fe-5Al alloys after FSW [17], the hardness increment is relatively small, likely due to DO_3 phase decomposition during FSW, which will be further discussed in the subsequent section.

3.3. Tensile properties

The room-temperature tensile curves of the SZ specimens of Fe-10Al and Fe-0.1C-10Al alloys are shown in Fig. 5a,b, respectively, with the corresponding tensile properties summarized in Fig. 5c. For reference, the tensile curves of Fe-xAl alloys (0.05, 2, and 5 wt% Al) and Fe-0.1C-xAl alloys (0.05 and 5 wt% Al) reported in a previous study [17] are also inserted in Fig. 5a,b. The nominal mechanical properties for various Al contents are listed in Table 1. The SZ specimen of the Fe-10Al alloy exhibits a yield strength (YS) of 626 MPa, an ultimate tensile strength of 684 MPa, and a high elongation of 40 %, together with substantial local elongation (L-El.). In contrast, the addition of 0.1 wt% C to Fe-10Al alloy enhances tensile strength, achieving a YS of 640 MPa and a UTS of 725 MPa, though total elongation (T-El.) slightly decreases to 38 % still

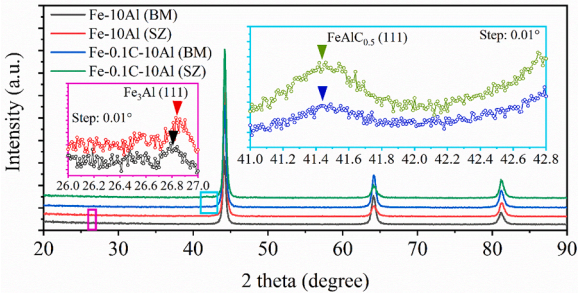

Fig. 3. XRD analysis of the BM and SZ regions of Fe-10Al and Fe-0.1C-10Al alloys; the inset shows a detailed scans of selected characteristic angular ranges for both alloys.

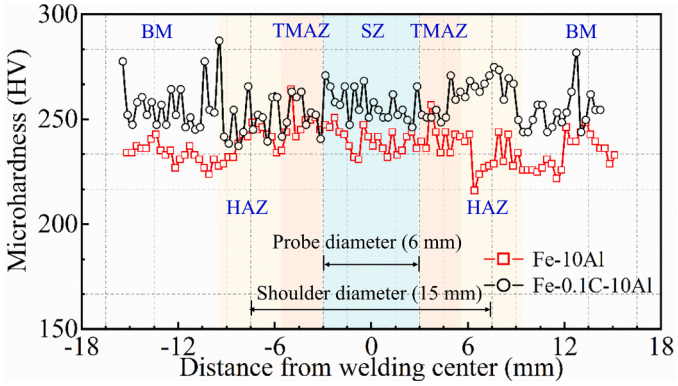

Fig. 4. Hardness distribution along the centerline through the thickness of the friction stir welded joints in Fe-10Al and Fe-0.1C-10Al alloys.

with large L-El.

Fig. 6 summarizes the mechanical properties (yield strength and elongation) of the base metals with Al contents below 5 wt% and increased to 10 wt%. It should be noted that the BMs were not homogenized prior to testing, and the results are presented for reference/comparison only. Despite the high Al content (10 wt%), both FSWed alloys with fine grain sizes exhibit an excellent balance of strength and ductility, which is completely different from the results of previous work [4]. The variations in strength and ductility of FSWed specimens with different Al contents are discussed in Section 4.3.1.

3.4. Fractography test

Fig. 7 presents the fracture morphologies of Fe-10Al and Fe-0.1C-10Al alloys after tensile testing, revealing distinct fracture behaviors influenced by composition and microstructural features. In Fe-10Al (Fig. 7a1), the fracture surface predominantly exhibits a ductile fracture mode, characterized by numerous equiaxed dimples (magnified micrographs Fig. 7a2). The presence of these dimples indicates significant plastic deformation prior to fracture. In contrast, the Fe-0.1C-10Al alloy exhibits a more complex fracture behavior, as shown in Fig. 7b1, c1, which displays fracture surfaces from two different regions of the same specimen, highlighting variations in local fracture morphology. The corresponding magnified images (Fig. 7b2,c2) reveal that both ductile and brittle fracture regions coexist in the Fe-0.1C-10Al alloy, indicating a mixed fracture mode. Notably, κ-carbides are embedded within some dimples, suggesting that carbide-matrix interactions influence the fracture mechanism. Additionally, secondary cracks are observed, particularly in Fig. 7c1, indicating that cracks presumably initiated in coarse κ-carbides and propagated into the matrix.

3.5. Impact toughness

The impact energy absorptions as a function of temperature for all SZs of Fe-10Al and Fe-0.1C-10Al specimens, obtained via miniature Charpy impact testing, are shown in Fig. 8a,b. The dimensions of the impact test specimens are illustrated in the inset of Fig. 2d. The upper shelf energy (USE) of the Fe-10Al alloy reaches approximately 390 ± 9 kJ/m², with a ductile-brittle transition temperature (DBTT) of approximately −15 ± 3°C. In contrast, the Fe-0.1C-10Al alloy shows an increased USE of 454 ± 5 kJ/m², while its impact toughness curve shifts to higher temperatures, resulting in a DBTT of approximately 70 ± 5°C. With increasing Al content, the USE increases while the DBTT also rises, following a trend consistent with previous studies on alloys with ≤ 5 wt % Al [17].

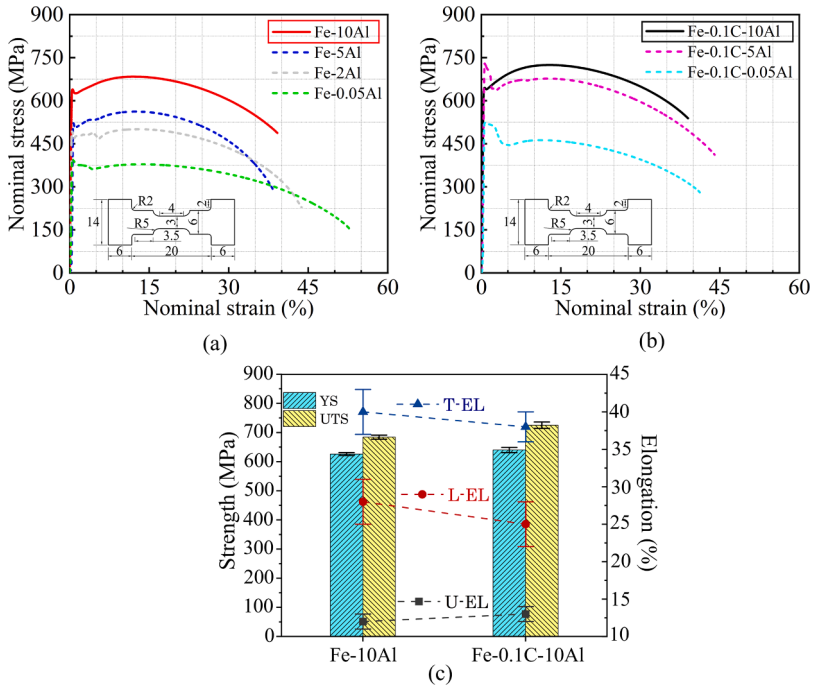

Fig. 5. Nominal stress–strain curves and corresponding histograms of strength and elongation for SZs. (a, b) The stress-strain curves of Fe-10Al and Fe-0.1C-10Al tensile specimens, respectively, inserted with the tensile stress-strain curves of Fe-xAl alloys (0.05, 2, and 5 wt% Al) and Fe-0.1C-xAl alloys (0.05 and 5 wt% Al) as reference [17]. (c) YS, UTS, U-EL, L-EL., and T-EL. of Fe-10Al and Fe-0.1C-10Al alloys; Strength values are plotted on the left axis, and elongation values on the right axis.

Table 1
Summary of the mechanical properties of FSWed specimens. The values are shown as the mean ± SD.

Material Type	Tensile properties				
	YS (MPa)	UTS (MPa)	U-El. (%)	L-El. (%)	T-El. (%)
Fe−0.05Al	361 ± 6	379 ± 6	14 ± 1	39 ± 2	53 ± 1
Fe−2Al	466 ± 4	501 ± 10	13 ± 1	31 ± 1	44 ± 1
Fe−5Al	532 ± 5	562 ± 7	13 ± 1	26 ± 2	39 ± 2
Fe−10Al	**626** ± 5	**684** ± 7	**12** ± 1	**28** ± 3	**40** ± 3
Fe-0.1C−0.05Al	445 ± 4	463 ± 11	11 ± 1	30 ± 1	41 ± 1
Fe-0.1C−5Al	636 ± 6	677 ± 5	13 ± 2	32 ± 2	45 ± 1
Fe-0.1C−10Al	**640** ± 9	**725** ± 11	**13** ± 1	**25** ± 3	**38** ± 2

4. Discussion

4.1. Decomposition of the order phase during friction stir welding

DO_3 represents a continuous ordered arrangement derived from the A2 structure. The high coherence between the ordered DO_3 structure and the matrix, similar to the relationship between the B2 ordered structure and its matrix [25]. Fig. 9a illustrates the selected location of the FIB-prepared TEM specimen in BM, supported by bright-field TEM image (Fig. 9b), as well as selected area electron diffraction (SAED) patterns (Fig. 9c) to confirm the DO_3 exist in Fe-10Al alloy. High-resolution TEM (HRTEM) images were acquired along the < 100 > zone axis (Fig. 9d1). A magnified view of the region in Fig. 9d1 is presented in Fig. 9d2. Diffraction patterns, derived from fast Fourier transform (FFT) analysis of the HRTEM image in Fig. 9d2, are shown in Fig. 9d3, accompanied by inverse FFT (IFFT1 and IFFT2) images for precise measurement of crystallographic spacing. Measurements

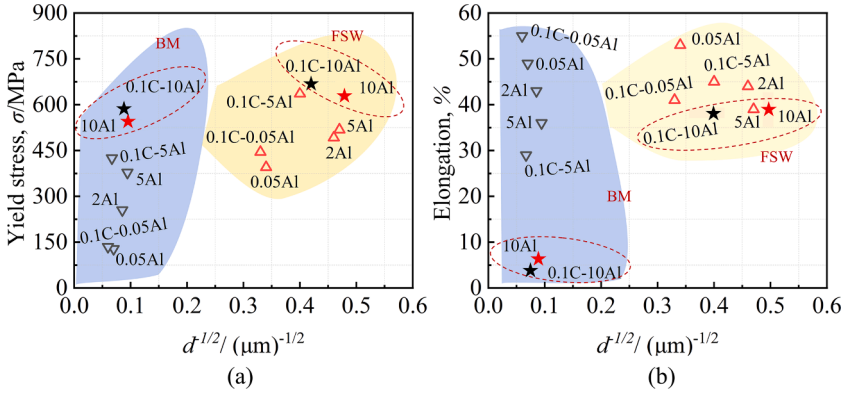

Fig. 6. Summary of yield strength and elongation for the BMs and SZs of all alloys involved in this study. (a) Yield strength of BM and SZ regions. (b) Elongation of BM and SZ regions. The dashed boxes in (a) and (b) highlight the performance at ~10 wt% Al. Data for Al contents below 5 % are taken from [17]. Note: Since all BMs were not homogenized, the basic mechanical properties of the BMs are provided for reference only.

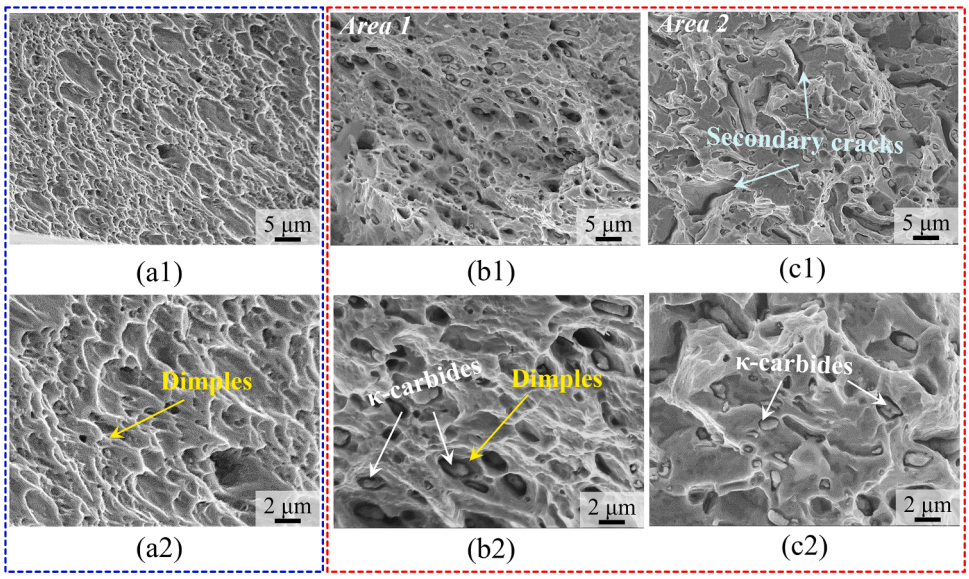

Fig. 7. Fracture morphologies after tensile testing. (a1) Fracture surface of Fe-10Al alloy, with (a2) as the magnified view of the selected region. (b1, c1) Fracture surfaces of Fe-0.1C-10Al alloy from different areas, with (b2) and (c2) as their respective magnified views.

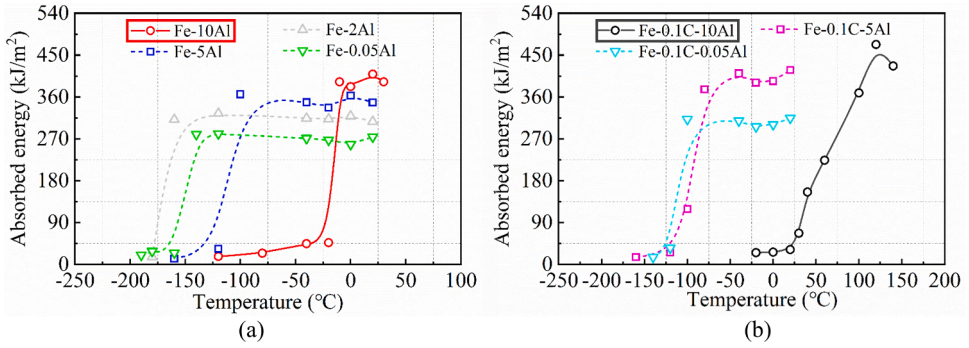

Fig. 8. Temperature dependence of the absorbed impact energies of the SZs. (a) Fe-10Al alloy. (b) Fe-0.1C-10Al alloy. The impact energy absorptions of alloys with Al content ≤ 5 wt% are shown as reference [17]. Grain size of Fe-xAl: 8.6 μm (0.05Al), 4.8μm (2Al), 4.6μm (5Al), 6.5μm (10Al); Grain size of Fe-0.1C-xAl: 9.1 μm (0.05Al), 6.2 μm (5Al), 6.1 μm (10Al).

indicate d1 ≈ 2.033 Å and d2 ≈ 3.113 Å, suggesting that the diffraction spots (Fig. 9d3) marked in red correspond to the BCC matrix, while the yellow-labeled diffraction spots align with Fe_3Al (DO_3), confirming its ordered structure.

The SZ of Fe-10Al FSWed joint exhibits distinct states for ordered phases. Analysis was conducted following the above approach, as shown in Figs. 10a,b,c1. FFT was applied to extract diffraction patterns from the enlarged view (Fig. 10c2) of HR image (Fig. 10c1). IFFT measurements of crystal spacing confirmed that the single diffraction pattern along the < 111 > zone axis, displayed in Fig. 10c3, corresponds to the ferrite matrix, with no evidence of superlattice arrays. This observation suggests that the introduction of significant dislocations accompanied by severe plastic strains, along with fractional heat input during the FSW process, likely induced the decomposition of DO_3 ordered structures. DO_3 presumably underwent an ordered-to-disordered transition during the FSW process. Combined with previous XRD analysis (Fig. 3), which confirmed the retention of characteristic DO_3 peaks in the SZ of the FSWed Fe-10Al alloy. However, the absence of diffraction spots corresponding to ordered phases at the selected locations suggests that partial decomposition of DO_3 occurred with a reduced volume fraction. Another important aspect to highlight is that short range order (SRO) serves as a precursor to the DO_3 phase, representing a local atomic ordering tendency. Given the thermo-mechanical effects introduced during FSW, it is reasonable to infer that, in addition to the $DO_3 \rightarrow A2$ transformation, a partial reversion of DO_3 to SRO also occurs. Furthermore, SRO is expected to be more prevalent in alloys with FSWed Fe-10Al specimens. Naturally, this behavior is assumed to be still present during FSW of Fe-0.1C-10Al alloy.

4.2. *Verification of the decomposition of the order phase during friction stir welding*

4.2.1. *Hardness variation during post weld heat treatment*

The hardness distribution in the SZ and BM serves as possible evidence supporting the partial decomposition of DO_3 during the FSW process. The lack of homogenization in the base material complicates the analysis. As a result, the contribution of grain refinement in SZ to these properties cannot be easily quantified using the Hall-Petch relationship [26]. Therefore, a direct comparison of hardness variation between the SZ and BM was performed for the Fe-10Al alloy with previously reported data for Fe-5Al alloy [17]. The Fe-5Al alloy exhibited a hardness increase of approximately 28 HV in the SZ compared to the BM due to the grain refinement. In contrast, the Fe-10Al alloy exhibited only a slightly higher hardness of 242 HV as compared to the hardness of BM (233 HV) as seen in Fig. 4. This slightly higher hardness of suggests that partial decomposition of the DO_3 phase occurred during FSW, which likely counteracts the hardness enhancement normally expected from grain refinement.

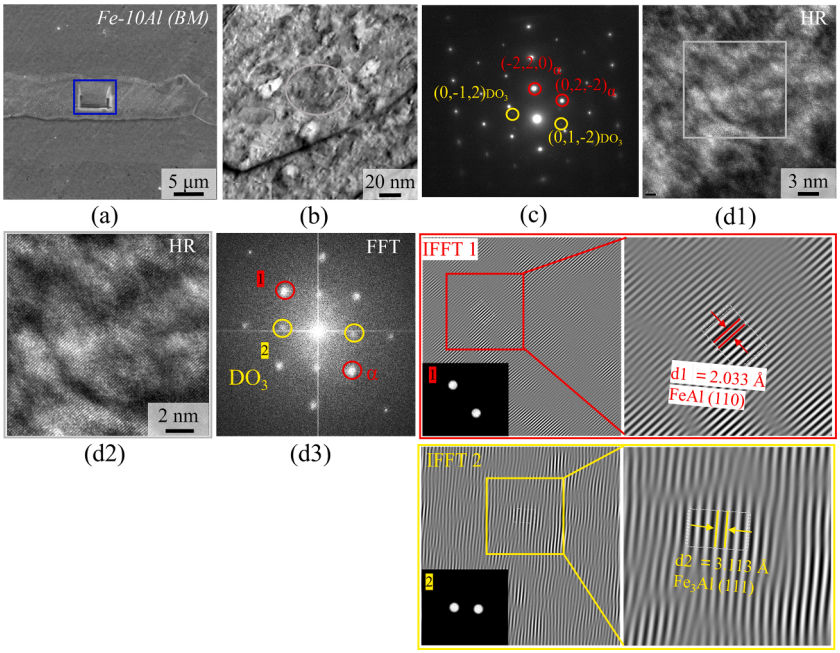

Fig. 9. Selection and analysis of the FIB-prepared TEM specimen from the BM of Fe-10Al alloy. (a) Location of the selected region for TEM analysis. (b, c) Bright-field TEM image and selected area electron diffraction (SAED) pattern, confirming the presence of the DO_3 phase in the Fe-10Al alloy. (d1) High-resolution (HR) TEM image along the < 100 > zone axis. (d2) Enlarged view of (d1). (d3) FFT diffraction pattern of (d2) with corresponding inverse FFT (IFFT1 and IFFT2) used for crystallographic spacing analysis.

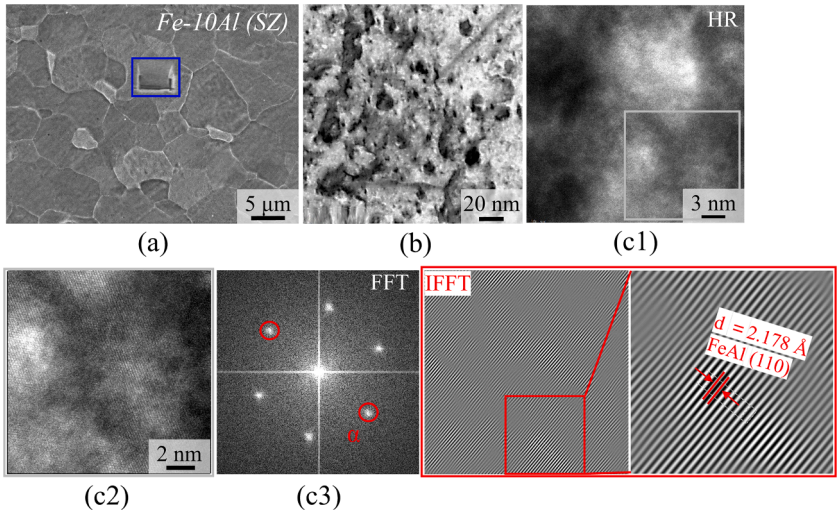

Fig. 10. Selection and analysis of the FIB-prepared TEM specimen from the SZ of FSWed Fe-10Al joint. (a) Location of the selected region for TEM analysis. (b) Bright-field TEM image. (c1) High-resolution (HR) TEM image. (c2) Enlarged view of (c1). (c3) FFT diffraction pattern of (c2) with corresponding inverse FFT image (IFFT) used for crystallographic spacing analysis.

The direct observation of the ordered DO_3 phase or its evolution during FSW is highly challenging [27,28]. Therefore, to validate this hypothesis, an isothermal aging treatment was conducted based on the known low-temperature formation characteristics of DO_3 exploiting Fe-Al phase diagram [29]. Specifically, Fe-Al specimens were aged at 400 °C for 24 h and 100 h, with non-aged as-FSWed specimens serving as a control group. The hardness distribution of the heat-treated specimens was subsequently evaluated, as shown in Fig. 11a,b. The results indicate that the hardness of the SZ in the specimens aged for 24 h increased by approximately 20 HV (8 %) compared to that of the non-heat-treated specimens. This observation confirms that the transformation from disordered A2 to ordered DO_3 presumably occurred during isothermal aging. The slight increase in microhardness after isothermal aging at 400 °C for 24 h provides supporting evidence for the decomposition of DO_3 during the FSW process. The slight decrease in hardness after 100 h aged specimen compared with 24 h aged specimen is attributed to the lattice misfit between the partially ordered phase and the matrix. Lattice misfit may cause weakening the bonding and strengthening effect, which leads to a slight decrease in hardness. Maji et al. [29] reported that a comparison of the hardness increment in specimens of Fe-12Cr-10Al alloy heat-treated at 475°C for different ageing times, indicates that the hardness variation induced by the DO_3 ordered phase can reach approximately ~30 HV, which suggests that evaluating the hardness evolution during post heat treatment is a reasonable approach to indirectly verify the decomposition of the DO_3 phase during the FSW process.

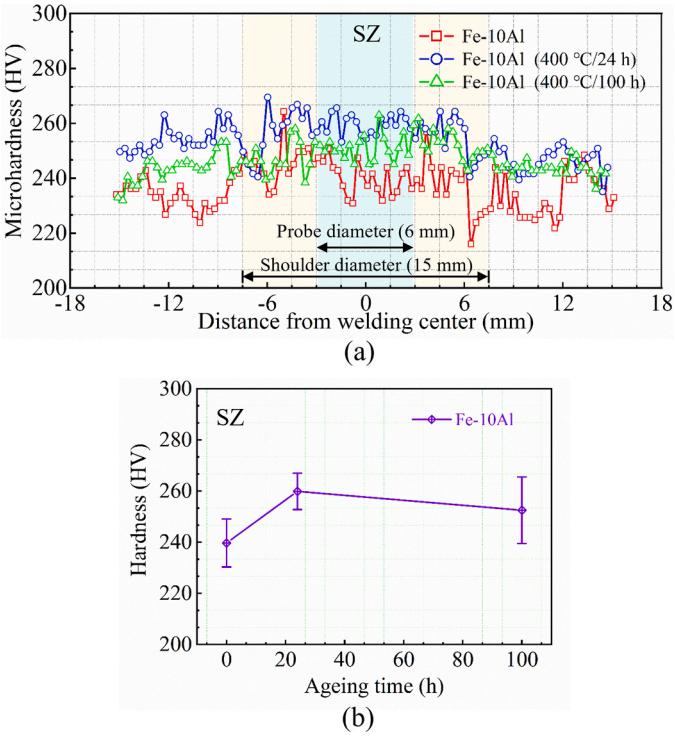

Fig. 11. Hardness distribution along the centerline through the thickness of Fe-10Al alloy aged at 400°C for different ageing times. (a) Hardness profiles of the as-welded specimen, the specimen aged at 400 °C for 24 h, and the specimen aged at 400 °C for 100 h. (b) Comparison of hardness values in the SZ of the three corresponding specimens. Error bars represent ±1σ (standard deviation).

4.2.2. *Verification of the order phase using solid solution hardening mechanism*

For Fe-xAl alloys, Al addition is known to enhance YS and hardness through solid solution hardening. In model alloys, the hardening effect is often proportional to $c^{1/2}$ [30] for low concentrated solute or $c^{2/3}$ [31] for high concentrated solute (where c is the solute concentration), while in engineering alloys, a linear relationship with c is typically observed [32,33]. Fig. 12 shows the variation of hardness with (Al wt%) $^{2/3}$. Up to 5 wt% Al, the data generally follows the expected trend; however, a marked deviation emerges at 10 wt%, suggesting an additional hardening mechanism beyond conventional solid solution effects. This deviation is assumed to be attributed to the transformation of the A2 matrix or localized SRO into the ordered phase DO_3 as Al content increases, whereby DO_3 contributes extra strengthening. During FSW, partial decomposition of the DO_3 phase likely occurs, attenuating its

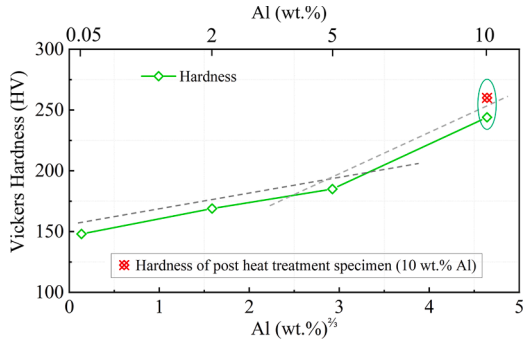

Fig. 12. Hardness of SZs as a function of Al content together with hardness of post heat treated Fe-10Al specimen. The green-framed area indicates the as-welded Fe-10Al specimen and the specimen after post-weld heat treatment at 400 °C for 24 h.

effect. This is supported by the post heat treated Fe-10Al specimens (red marker in Fig. 12) as discussed in 4.2.1, where recovery of DO_3 leads to a significant hardness increase compared to the as-welded condition, confirming that DO_3 in BM partially decomposes during FSW.

4.2.3. *Dislocation structure*

The dislocation structures in Fe-10Al tensile specimens, subjected to ~5 % tensile strain, both in the as-welded and post heat treated (400°C for 24 h) conditions, were investigated as shown in Fig. 13. In the as-welded condition, linear dislocations like straight lines are introduced into the deformed ferrite within the SZ, exhibiting an apparent interwoven and network-like distribution. In some localized regions, dislocation lines are arranged in a relatively ordered manner, indicating a crystallographic slip system, as shown in Fig. 13a1 and the magnified view of the selected area in Fig. 13a2,a3. During tensile deformation, multiple slip systems are activated, and the possible presence of SRO in the matrix exerts a drag effect on dislocations [34]. The dislocation motion is constrained, with some dislocations showing a tendency to form entanglements. The localized effect of SRO on dislocation motion is primarily attributed to atomic-scale energy barriers that disrupt linear slip, leading to the formation of antiphase boundaries (APBs). However, since the influence of SRO is limited to short-range interactions, the overall complexity of dislocation movement remains moderate. Some dislocations are able to locally overcome these energy barriers, displaying partial slip behavior. It is well established that SRO can be sheared by dislocations, with the first dislocation experiencing significant resistance while subsequent dislocations encounter markedly reduced obstacles [35]. This implies that in certain regions, dislocations may overcome APB-related barriers and continue their movement, albeit in a restricted manner. Given the localized nature of SRO pinning effect, dislocations in less constrained regions can still traverse a certain distance along crystallographic slip planes, leading to relatively sparse or liner dislocation structures in some TEM observations.

In contrast, the dislocation structure in the post heat treated specimen after 24 h at 400°C is significantly more complex, with a further increase in dislocation density and the emergence of pronounced dislocation bending and entanglement, as shown in Fig. 13b1 and magnified view of selected area in Fig. 13b2,b3. Regional dislocation interactions and pile-ups are evident, indicating more severe constraints on dislocation motion. This confirms the transformation from A2 and SRO to DO_3 ordering during post heat treatment. The formation and increased fraction of the DO_3 ordered phase enhance long-range ordering effects, leading to a stronger pinning effect on dislocations. As a stable long-range ordered structure in ferrite, DO_3 exerts a well-documented, more extensive influence than SRO on dislocation movement, further restricting dislocation glide and recovery. This effect ultimately manifests as more intricate dislocation pile-ups and highly interwoven distributions, as shown in Fig. 13b3. These findings corroborate the partial transformation of DO_3 to A2 and SRO during FSW and recovery of DO_3 after post heat treatment.

4.3. *Deformation behaviors of stir zones in friction stir welded Fe-10Al and Fe-0.1C-10Al alloys*

4.3.1. *Strength-ductility*

The high YS and moderate strain-hardening capacity of the SZ specimen of the FSWed Fe-10Al alloy primarily originate from a substantial increase in friction stress associated with solid solution strengthening [36], as well as from grain refinement induced by dynamic recrystallization during FSW. Moreover, the high Al content promotes the formation of SRO and the ordered DO_3 phase, which further contribute to the enhancement of both yield and tensile strength. Importantly, the FSWed alloys exhibit good ductility, as illustrated in Fig. 5, particularly in terms of good L-El., which is a completely different result from previous one [4,37]. Grain refinement achieved through dynamic recrystallization by FSW is considered the primary factor

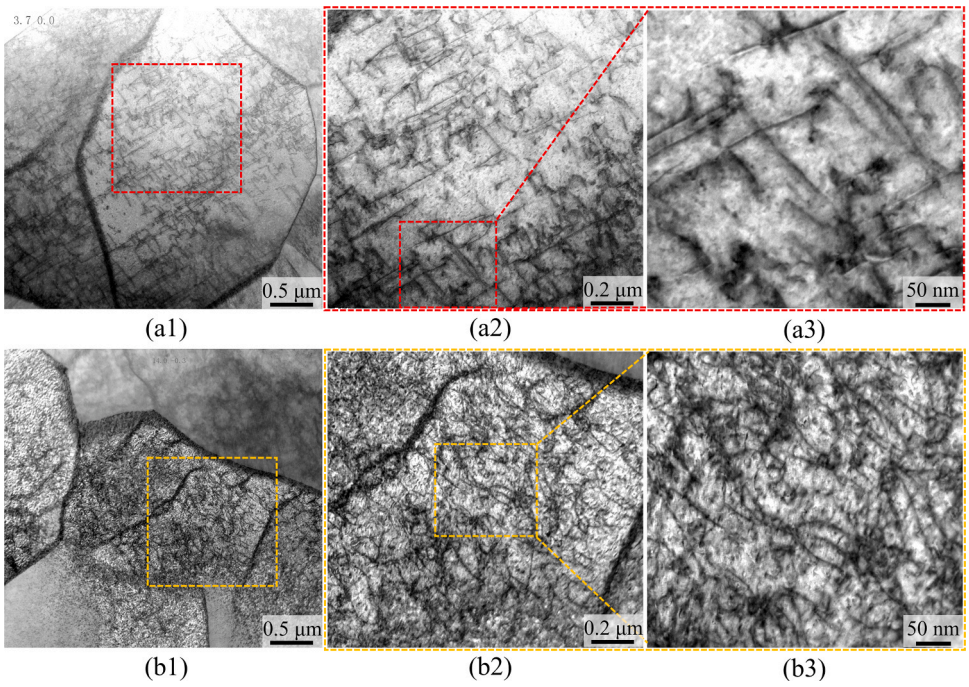

Fig. 13. TEM micrographs show the dislocation structure after ~5 % tensile strain. (a1–a3) Fe-10Al in as-FSWed state without aging treatment, with increasing magnification from (a1) to (a3). (b1–b3) Fe-10Al in subsequently aged (400 ℃ for 24 h) state, with increasing magnification from (b1) to (b3).

responsible for the significant improvement in L-El., as it mitigates strain localization, enhances resistance to fracture-induced strain localization, and effectively suppresses void growth [22]. At identical FSW parameters, the grain sizes in the SZs are comparable across different Al concentrations. Furthermore, even with an Al content as high as 10 wt%, the specimen still exhibits good ductility. In addition to the contribution from grain refinement, this retention of ductility is also presumed to be attributed to the partial decomposition of the DO_3 phase during FSW, which is speculated to alleviate the pinning effect of the ordered phase on dislocation motion. The L-El. of SZ in Fe-10Al reaches approximately 28 %. Typically, according to the previous report [37], when Al content approaches 10 wt%, L-El. is nearly zero.

In Fe-0.1C-10Al, besides grain refinement, the effects of DO_3 decomposition and interactions between κ-carbides and dislocations must be considered for mechanical performance. TEM analysis of the SZ in FSWed specimen is shown in Fig. 14. Fig. 14a shows κ-carbide in the BM region, where a small number of dislocations are observed inside, suggesting that slight plastic deformation of the κ-carbides may have

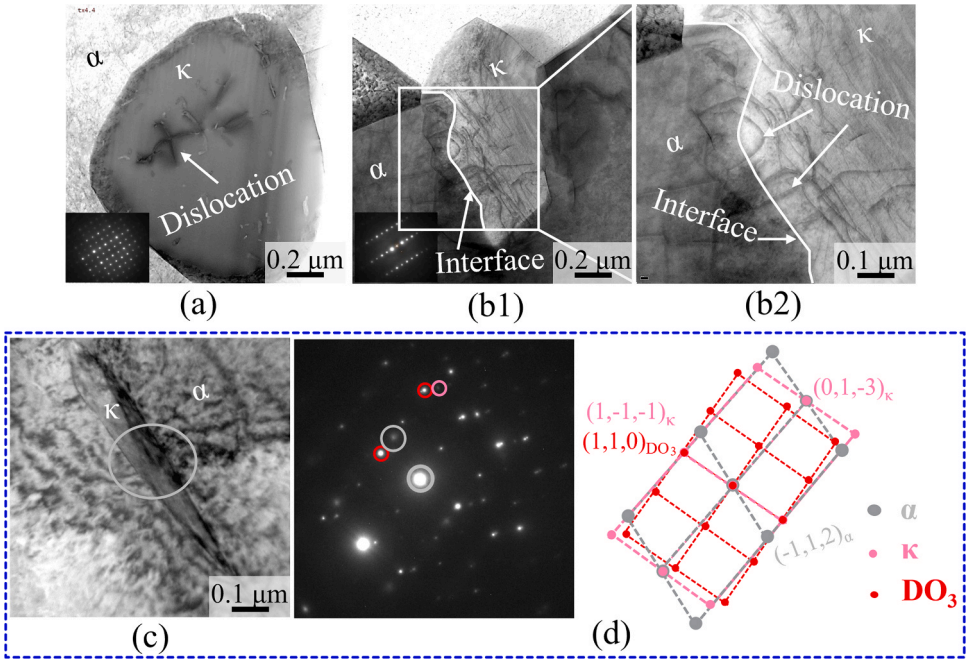

Fig. 14. TEM characterization of carbides in the BM and SZ of Fe-0.1C-10Al alloy. (a) Bright-field TEM image of κ-carbide in the BM. (b1) Bright-field TEM image of a region containing large κ-carbide of SZ; (b2) Magnified view of the selected area in (b1); (c) Bright-field TEM image of fine κ-carbide; (d) Selected area diffraction pattern of (c), with corresponding the schematic.

occurred during hot rolling. After FSW, bright-field TEM image reveals the presence of large κ-carbides retained from the BM (Fig. 14b1) and fine κ-carbides precipitated at grain boundaries (Fig. 14c). Large κ-carbides undergo significant plastic deformation during FSW, as shown in Fig. 14b2. A high density of dislocations is introduced within κ-carbides, whereas dislocation accumulation on the ferrite matrix side is minimal. Some dislocations penetrate the ferrite/κ-carbide interface, as seen in the region highlighted in Fig. 14b1, with a magnified view provided in Fig. 14b2. These observations confirm that high-density dislocations shear the κ-carbides through a cutting-through mechanism, consistent with the Friedel effect [13]. During the shearing process, dislocations "capture" carbon atoms, which are then presumably transferred to the ferrite matrix. These escaped carbon atoms diffuse to grain boundaries and precipitate as fine κ-carbides (Fig. 14c). This behavior was previously observed in FSWed Fe-0.1C-5Al, where the relatively lower Al content led to the diffusion of carbon atoms to the grain boundaries, resulting in the precipitation of fine cementite [11]. The cutting-through mechanism leaves behind numerous dislocation remnants within κ-carbides, serving as dislocation sources for further deformation [38]. Notably, fine cementite precipitates at grain boundaries in Fe-0.1C-5Al, while κ-carbides are instead precipitated in Fe-0.1C-10Al due to the higher Al content. Additionally, bright-field TEM images (Fig. 14c), selected area diffraction patterns with the schematic (Fig. 14d) reveal weak superlattice reflections corresponding to the DO_3 phase around fine κ-carbides. The presence of ordered DO_3 in the vicinity of κ-carbides is reasonable, given that carbon depletion at grain boundaries favors ordered phase formation. This confirms that not all DO_3 decomposes into SRO or A2 during FSW and some of the DO_3 remain intact. The stress relaxation caused by the dislocation cutting through mode, coupled with the partial transformation of DO_3 into SRO or disordered A2, collectively enables the FSWed Fe-0.1C-10Al alloy to maintain good plasticity despite its high strength. A slight decrease in L-El. is expected due to DO_3 and κ-carbide in Fe-0.1C-10Al.

4.3.2. *Plastic deformation mechanism of stir zone in friction stir welded Fe-10Al alloy*

The increase in Al content promotes the formation of ordered phases, which restrict dislocation motion and increase the likelihood of deformation twinning. In BCC crystals, reduced screw dislocation mobility is a prerequisite for twinning [39,40]. A study [37] observed deformation twins in the deformed region of an Fe-18 at% Al (~9 wt%) alloy with a grain size of ~1 mm. It was also reported that increasing Al content reduces dislocation mobility, leading to lower fracture strain. This suggests that Fe-Al alloys with ~10 wt% Al tend to exhibit deformation twinning at the fracture area [41]. However, in the FSWed Fe-10Al alloy examined here, no deformation twins were found in the fractured area after tensile testing (Fig. 15a,b). If dislocation motion is more constrained under the low temperature and high strain rate conditions, deformation twinning—typically a rapid response mechanism—is presumed more likely to occur.

The fracture surface of the SZ in FSWed Fe-10Al after Charpy impact testing at –40 °C was analyzed (Fig. 15c, with magnified views in Fig. 15d1,d2), but no deformation twins were observed in the fractured grains. This absence may be related to the effect of grain size on deformation modes. In coarse-grained alloys with fewer grain boundaries, deformation concentrates in fewer grains, causing stress localization at grain boundaries. When slip alone is insufficient, twinning is more easily activated to transfer strain [40]. In contrast, the refined SZ in the FSWed Fe-10Al alloy has the higher density of grain boundaries which facilitate stress redistribution, reducing local stress concentrations and favoring deformation via dislocation slip over twinning. The effect of grain size on deformation twinning in Fe-10Al is under investigation and will be reported soon.

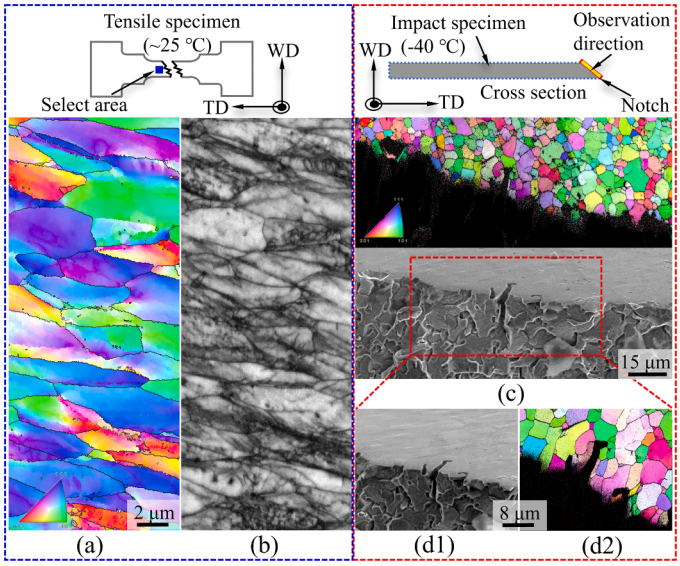

Fig. 15. EBSD analysis of the fractured specimens in the SZ of FSWed Fe-10Al alloy. (a, b) Inverse Pole Figure (IPF) map and Image Quality (IQ) map of the tensile specimen near the fracture surface. (c) SEI morphology and corresponding IPF map of the impact specimen fractured surface at −40℃, with (d1) and (d2) showing magnified SEI images and IPF map of the selected regions in (c).

4.4. *Toughness*

During deformation, some dislocations shear the SRO or ordered DO_3 lattice. If this process alters atomic positions and disrupts the original order, it forms APBs. APBs have high energy and increase brittleness, facilitating crack initiation and propagation. The APB energy is directly related to the degree of ordering. The higher the order, the greater the disruption caused by APB formation. Thus, in FSWed high-Al alloys with a high fraction of SRO and/or long-range ordered DO_3, the APB energy is high, which aligns with the increase in DBTT as Al content rises in Fe-xAl alloys. The energy absorption capacity of Fe-0.05Al, Fe-5Al, and Fe-10Al alloys at −40°C were compared based on the load-displacement curves of Charpy impact tests, as shown in Fig. 16a. Charpy impact test data at −40°C indicate that Fe-0.05Al and Fe-5Al alloys exhibit ductile fracture [17], whereas Fe-10Al undergoes brittle fracture. The impact fracture surface morphology of Fe-10Al alloy at −40 ℃ is shown in Fig. 16b. In Fe-10Al, crack initiation and propagation occur within the ferrite matrix under low loads, as shown in Figs. 16b and 17. A similar crack morphology was observed in Fe-5Al Charpy impact tested at −160 °C [17]. The fracture surface of Fe-10Al tested at −40 ℃ mainly exhibited transgranular cleavage as shown in Fig. 17, which indicates that the

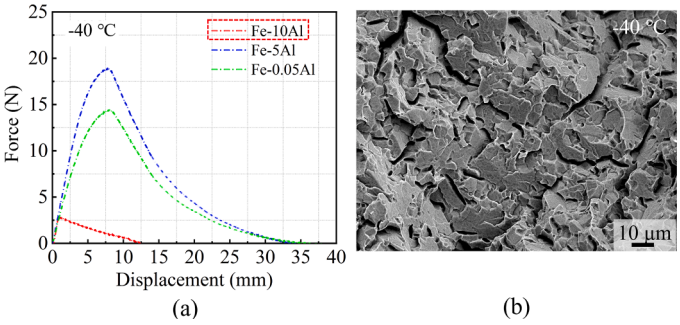

Fig. 16. Low-temperature (-40 ℃) Charpy impact performance of Fe-Al alloys. (a) Comparison of energy absorption capacity of Fe-0.05Al, Fe-5Al, and Fe-10Al alloys at −40°C. (b) Fracture surface morphology of Fe-10Al alloy after impact testing at –40 °C.

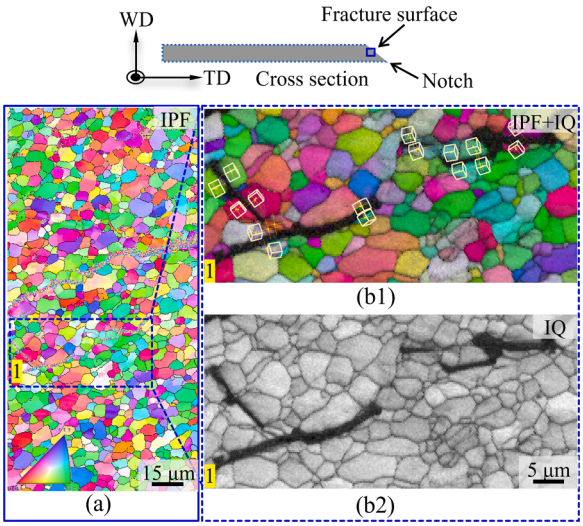

Fig. 17. Crack initiation and propagation near the fracture surface of Charpy impact specimens of Fe-10Al alloy at −40°C. (a) IPF of selected area. (b1) Enlarged map of IPF+IQ for area 1, including crystallographic orientation analysis of the crack region, showing cleavable {100} crystal planes. (b2) Enlarged map of IQ for area 1.

crack propagates primarily along the easily cleavable {100} crystal planes, which may be related to the ordered DO_3 phases or SRO. This embrittlement is attributed to localized ordering within the matrix at high Al content, which is also considered a major reason for the significant shift of the DBTT toward higher temperatures in the Fe-10Al alloy.

Tanaka et al. [42] reported that twin-twin intersections were seen in fracture surfaces in Fe-8 wt% Al single crystal after Charpy impact test at −14 °C, where the applied tensile stress was along [100] around the notch, and concluded that the intersection of deformation twins was the origin of a brittle fracture. In the present study, no clear deformation twin was observed near the sub-crack region as shown in Fig. 17. Combined with the fact that no deformation twin was also found in the grain at the brittle fracture surface (Fig. 15c), the importance of grain size affecting twin formation is indicated as discussed in Section 4.3.2.

In the FSWed Fe-0.1C-10Al alloy, a substantial increase in DBTT, which is approximately 75 ± 3 °C, manifested room-temperature brittleness. In addition to DO_3 and SRO, coarse κ-carbides present are accelerating crack nucleation, resulting from not only exceeding κ-carbide deformation limit but also κ-carbide decohesion from the matrix under deformation. Furthermore, the presence of fine κ-carbides at grain boundaries may also have contributed to this behavior. Tensile fracture surface analysis revealed the formation of voids and secondary cracks associated with both coarse and fine κ-carbides, as shown in Fig. 7c1,c2. These combined factors contribute to the easy initiation and rapid propagation of cracks in Fe-0.1C-10Al under loading. Therefore, in the SZ of FSWed Fe-0.1C-10Al, where κ-carbides are present, these carbides play a dominant role in determining the fracture mode, distinguishing it from the Fe-10Al alloy without carbon. DBTT suddenly increased due to the strong negative effect of simultaneous existence of DO_3 and κ-carbide is speculated. Notably, despite the high DBTT, Fe-0.1C-10Al exhibits relatively high impact energy absorption and good impact resistance at elevated temperatures.

The results obtained in the present study by exploiting unique FSW process at low temperatures suggest the guiding principle to manufacture significantly high-Al steel products with excellent properties by reducing grain size of about 5–6 μm together with decomposed DO_3 and shearable κ-carbides. In fact, the FSW strategy—distinguished by its extremely low rotation rate and high axial load—offers practical advantages for engineering applications. In addition to high-Al ferritic steels, this approach can likewise be extended to other metallic systems containing brittle second-phase constituents, such as coarse precipitates or intermetallic compounds (IMCs). It promotes their fragmentation, refined distribution, or even partial dissolution through thermo-mechanical effects, accompanied by grain refinement without phase transformation (below A_1), all of which contribute positively to strength, ductility and toughness. The FSW-based method only requires precise adjustment of parameters within the below A_1 temperature range of target alloys to achieve the above effects. Moreover, it naturally integrates the welding capability that is essential for structural applications of metallic materials, offering a reliable joint formation.

5. Conclusions

High-quality joints of Fe-10Al and Fe-0.1C-10Al alloys were successfully fabricated by FSW under extremely low rotational rate and systematically investigates the microstructural evolution and mechanical properties of FSWed Fe-10Al and Fe-0.1C-10Al alloys. Particular attention is given to the decomposition of ordered phases and the shearability of κ-carbides, as well as their effects on tensile properties, toughness, and crack initiation and propagation. The key findings are as follows:

1. The increase in Al content to 10 wt% promotes the formation of ordered phase of DO_3, leading to a reduction in dislocation mobility. This generally enhances the likelihood of deformation twinning in coarse-grained Fe-Al alloys; however, in FSWed fine-grained microstructures of SZ, deformation during tensile test occurs primarily via dislocation slip due to the stress redistribution at grain boundaries leading to excellent ductility and reasonable toughness.
2. During FSW, DO_3 decomposes, order DO_3→disorder A2, with some residual SRO remaining locally in a smaller size. Despite the refined ferrite grains in the SZ of Fe-10Al and Fe-0.1C-10Al, the hardness only slightly increases compared to the BM—by about 9 HV and 12 HV, respectively.
3. The SZs of both alloys exhibit high ductility due to the grain refinement effect, especially in terms of local elongation, reaching 28 % and 25 % for SZs of Fe-10Al and Fe-0.1C-10Al, respectively—superior to previously reported. For the Fe-10Al, the decomposition of the DO_3 phase during FSW is another reason for good ductility, as the reduced dislocation pinning effect facilitates easier slip. For the Fe-0.1C-10Al, in addition to the decomposition of DO_3, dislocations cutting through the κ-carbides during FSW lead to stress relaxation, ultimately enhancing ductility.
4. With increasing Al content (10 wt%), the presence of SRO and DO_3 ordering raises the anti-phase boundary energy, facilitating crack initiation and propagation, contributing to a higher DBTT. The DBTT in the SZ of Fe-10Al reaches −15 °C, while that of Fe-0.1C-10Al rises to 70 °C. For Fe-10Al, the brittle fracture surface impact-tested at low temperature mainly exhibits transgranular cleavage, which indicates that the crack propagates primarily along the easily cleavable {100} crystal planes, which may be related to the ordered DO_3 phases or SRO. The further reduced toughness of Fe-0.1C-10Al compared to Fe-10Al is mainly attributed to κ-carbides, which serve as crack initiation sites and promote crack propagation.
5. The present study exploiting unique FSW process at low temperatures with high axial load suggests the guiding principle to manufacture significantly high-Al steel products with excellent properties.

CRediT authorship contribution statement

Chen Junqi: Writing – original draft, Validation, Software, Methodology, Investigation, Formal analysis, Data curation, Conceptualization. **Takuya Miura:** Writing – review & editing, Visualization, Supervision, Methodology, Investigation. **Kohsaku Ushioda:** Writing – review & editing, Visualization, Supervision, Conceptualization. **Abhishek Sharma:** Writing – review & editing. **Hidetoshi Fujii:**

Writing – review & editing, Supervision, Project administration, Funding acquisition, Conceptualization.

Declaration of Competing Interest

We declare that we have no financial and personal relationships with other people or organizations that can inappropriately influence our work, there is no professional or other personal interest of any nature or kind in any product, service and/or company that could be construed as influencing the position presented in, or the review of, the manuscript entitled.

Acknowledgments

This work was supported by the JST-Mirai Program Grant Number JPMJMI19E5 and JSPS KAKENHI Grant Number JP19H00826, JP23K13576. The authors appreciate the financial support of the ISIJ Research Project of The Iron and Steel Institute of Japan, and China Scholarship Council, grant no. 202308050076.

Data Availability

The raw/processed data required to reproduce these findings cannot be shared at this time as the data also forms part of an ongoing study.

References

[1] Chen, S., Rana, R., Haldar, A., Ray, R.K., 2017. Current state of Fe-Mn-Al-C low density steels. Prog. Mater. Sci. 89, 345–391. https://doi.org/10.1016/j.pmatsci.2017.05.002.
[2] Czerwinski, F., 2021. Current trends in automotive lightweighting strategies and materials. Materials 14, 6631. https://doi.org/10.3390/ma14216631.
[3] Brüx, U., Frommeyer, G., Jimenez, J., 2002. Light-weight steels based on iron aluminium-influence of micro alloying elements (B, Ti, Nb) on microstructures, textures and mechanical properties. Steel Res. 73, 543–548. https://doi.org/10.1002/srin.200200026.
[4] Herrmann, J., Inden, G., Sauthoff, G., 2003. Deformation behaviour of iron-rich iron-aluminium alloys at low temperatures. Acta Mater. 51, 2847–2857. https://doi.org/10.1016/S1359-6454(03)00089-2.
[5] Frommeyer, G., Habrock, H.J., Wittig, J.E., Geenen, J., Kreuss, M., 1990. Investigations on phase transformations and B2-DO_3 superlattices in ordered iron aluminium alloys by FIM — atom probe and TEM. Scr. Met. 24, 51–56. https://doi.org/10.1016/0956-716X(90)90565-X.
[6] Stoloff, N.S., 1998. Iron aluminides: present status and future prospects. Mater. Sci. Eng. A 258, 1–14. https://doi.org/10.1016/S0921-5093(98)00909-5.
[7] Morris, D.G., Garcia Oca, C., Chao, J., Munoz-Morris, M., 2002. Influence of machining conditions on tensile stress and ductility of a mechanically alloyed Fe-40Al intermetallic. Scr. Mater. 46, 843–850. https://doi.org/10.1016/S1359-6462(02)00063-5.
[8] Yoshimi, K., Saeki, Y., Yoo, M.H., Hanada, S., 1998. Room temperature tensile properties of Fe-Al single crystals strengthened by excess vacancies. Mater. Sci. Eng. A 258, 75–83. https://doi.org/10.1016/S0921-5093(98)00920-4.
[9] Morris, D.G., Gunther, S., 1996. Order-disorder changes in Fe3Al based alloys and the development of an iron-base α-α″ superalloy. Acta Mater. 44, 2847–2859. https://doi.org/10.1016/1359-6454(95)00382-7.
[10] Marcinkowski, M.J., Taylor, M.E., Kayser, F.X., 1975. Relationship between atomic ordering and fracture in Fe-Al alloys. J. Mater. Sci. 10, 406–414. https://doi.org/10.1007/BF00543684.
[11] Chen, J., Miura, T., Ushioda, K., Fujii, H., 2025. Elucidating deformation behavior of cementite and κ-carbide during friction stir welding of Fe-0.1C-xAl (x = 0.05 and 5 mass%) steels below A_1. Mater. Charact. 225, 115205. https://doi.org/10.1016/j.matchar.2025.115205.
[12] Courtney, T.H., 2005. Mechanical Behavior of Materials. Waveland Press.
[13] J.K. Lopez Barrilao, T. Beck, L. Singheiser, Lehrstuhl für Werkstoffe der Energietechnik (FZ Jülich), PhD Dissertation, 2017. https://doi.org/10.18154/RWTH-2017-01982.
[14] Xiong, Z., Timokhina, I., Pereloma, E., 2020. Clustering, nano-scale precipitation and strengthening of steels. Prog. Mater. Sci. 115, 100764. https://doi.org/10.1016/j.pmatsci.2020.100764.
[15] Jiang, S., Wang, H., Wu, Y., Liu, X., Chen, H., Yao, M., 2017. Ultrastrong steel via minimal lattice misfit and high-density nanoprecipitation. Nature 544, 460–464. https://doi.org/10.1038/nature22032.
[16] Xue, H., Yang, C., De Geuser, F., 2023. Highly stable coherent nanoprecipitates via diffusion dominated solute uptake and interstitial ordering. Nat. Mater. 22, 434–441. https://doi.org/10.1038/s41563-022-01420-0.
[17] Chen, J., Miura, T., Ushioda, K., Fujii, H., 2025. Microstructures and mechanical properties of FSWed Fe-xAl and Fe-0.1C-xAl alloys. J. Mater. Res. Technol. 36, 888–902. https://doi.org/10.1016/j.jmrt.2025.03.140.
[18] Huang, Y.W., Tung, P.C., Wu, C.Y., 2007. Tuning PID control of an automatic arc welding system using a SMAW process. Int. J. Adv. Manuf. Technol. 34, 56–61. https://doi.org/10.1007/s00170-006-0569-4.
[19] Chou, C.P., Lee, C.H., 1990. Effect of carbon on the weldability of Fe-Mn-Al alloys. J. Mater. Sci. 25, 1491–1496. https://doi.org/10.1007/BF00585471.
[20] Ku, J.S., Ho, N.J., Tjong, S.C., 1993. Properties of electron-beam-welded and laser-welded austenitic Fe-28Mn-5Al-1C alloy. J. Mater. Sci. 28, 2808–2814. https://doi.org/10.1007/BF00356223.
[21] Tjong, S.C., Zhu, S.M., Ho, N.J., Ku, J.S., 1997. Solidification microstructure and creep rupture behaviour of electron beam welded austenitic Fe-28Mn-6Al-1C alloy. Mater. Sci. Technol. 13, 251–256. https://doi.org/10.1179/mst.1997.13.3.251.
[22] Park, M.H., Tagusari, Y., Tsuji, N., 2022. Characterization of local deformation and fracture behavior in ferrite + martensite dual-phase steels having different grain sizes. IOP Conf. Ser. Mater. Sci. Eng. 1249, 012041. https://doi.org/10.1088/1757-899X/1249/1/012041.
[23] Chen, J., Miura, T., Ushioda, K., Fujii, H., 2024. Effects of microstructure and phosphorus segregation on tensile properties of friction stir welded high phosphorus weathering steel. Mater. Sci. Eng. A 916, 147315. https://doi.org/10.1016/j.msea.2024.147315.
[24] Vic-3D-8, Correlated Solutions, December, 2020. ⟨https://www.correlatedsolutions.com/software-downloads/#vic3d⟩.
[25] Jeong, S., Kim, B., Moon, J., Park, S.J., Lee, C., 2018. Influence of κ-carbide precipitation on the microstructure and mechanical properties in the weld heat-affected zone in various FeMnAlC alloys. Mater. Sci. Eng. A 726, 223–230. https://doi.org/10.1016/j.msea.2018.04.088.
[26] Naik, S.N., Walley, S.M., 2020. The Hall–Petch and inverse Hall-Petch relations and the hardness of nanocrystalline metals. J. Mater. Sci. 55, 2661–2681. https://doi.org/10.1007/s10853-019-04160-w.
[27] Chen, S., Aitken, Z.H., Pattamatta, S., 2021. Simultaneously enhancing the ultimate strength and ductility of high-entropy alloys via short-range ordering. Nat. Commun. 12, 4953. https://doi.org/10.1038/s41467-021-25264-5.
[28] Yan, Y.Q., Cha, W.H., Liu, S., 2025. Ductilization of 2.6-GPa alloys via short-range ordered interfaces and supranano precipitates. Science 387, 401–406. https://doi.org/10.1126/science.adr4917.
[29] Maji, B.C., Ukai, S., Oono-Hori, N., 2021. Microstructural stability and intermetallic embrittlement in high Al containing FeCrAl-ODS alloys. Mater. Sci. Eng. A 807, 140858. https://doi.org/10.1016/j.msea.2021.140858.
[30] Fleischer, R.L., 1963. Substitutional solution hardening. Acta Met. 11, 203–209. https://doi.org/10.1016/0001-6160(63)90213-X.
[31] Labusch, R., 1972. Statistical theories of solid solution hardening. Acta Met. 20, 917–927. https://doi.org/10.1016/0001-6160(72)90085-5.
[32] R. Sandstrom, Solid Solution Hardening, In: Basic Modeling and Theory of Creep of Metallic Materials 339, 2024, pp. 115-129. https://doi.org/10.1007/978-3-031-49507-6_6.
[33] Sieurin, H., Zander, J., Sandstrom, R., 2006. Modelling solid solution hardening in stainless steels. Mater. Sci. Eng. A 415, 66–71. https://doi.org/10.1016/j.msea.2005.09.031.
[34] Schön, C.G., 2021. On short-range order strengthening and its role in high-entropy alloys. Scr. Mater. 196, 113754. https://doi.org/10.1016/j.scriptamat.2021.113754.
[35] Schön, C.G., Kikuchi, R., 2001. Cluster variation method for determining the energy of slip-induced anti-phase boundary in BCC alloys. Theor. Appl. Fract. Mech. 35, 243–254. https://doi.org/10.1016/S0167-8442(01)00048-9.
[36] Wang, F., Song, M., Elkot, M.N., 2024. Shearing brittle intermetallics enhances cryogenic strength and ductility of steels. Science 384, 1017–1022. https://doi.org/10.1126/science.ado2919.
[37] Herrmann, J., Inden, G., Sauthoff, G., 2003. Deformation behaviour of iron-rich iron-aluminum alloys at low temperatures. Acta Mater. 51, 2847–2857. https://doi.org/10.1016/S1359-6454(03)00089-2.
[38] Li, B.Q., Beyerlein, I.J., Shinzato, S., 2024. Mechanism of solute hardening and dislocation debris-mediated ductilization in Nb-Si alloy. J. Mater. Sci. Technol. 203, 167–179. https://doi.org/10.1016/j.jmst.2024.03.052.
[39] Khaple, S., Golla, B.R., Prasad, V.V.S., 2023. A review on the current status of Fe–Al based ferritic lightweight steel. Def. Technol. 26, 1–22. https://doi.org/10.1016/j.dt.2022.11.019.
[40] Mahajan, S., Williams, D.F., 1973. Deformation twinning in metals and alloys. Int. Metall. Rev. 18, 43–61. https://doi.org/10.1179/imtlr.1973.18.2.43.
[41] Frommeyer, G., Drewes, E.J., Engl, B., 2000. Physical and mechanical properties of iron-aluminium-(Mn, Si) lightweight steels. Rev. MéTall 97, 1245–1253. https://doi.org/10.1051/METAL:2000110.
[42] Tanaka, M., Maeno, K., Higashida, K., Fujikura, M., Ushioda, K., 2011. The increase in a brittle-to-ductile transition temperature in Fe-Al single crystal. ISIJ Int 51, 999–1004. https://doi.org/10.2355/isijinternational.51.999.